ELSEVIER

Journal of Applied Geophysics 44 (2000) 85–102

JOURNAL OF APPLIED GEOPHYSICS

www.elsevier.nl/locate/jappgeo

# Cross-hole electrical imaging of a controlled saline tracer injection

L. Slater [a,*,1], A.M. Binley [b,2], W. Daily [c,3], R. Johnson [d,4]

[a] *Department of Geosciences, University of Missouri-Kansas City, 5100 Rockhill Road, Kansas City, MO 64110, USA*

[b] *Department of Environmental Science, Institute of Environmental and Natural Sciences, Lancaster, LA1 4YQ, UK*

[c] *Lawrence Livermore National Laboratory, Livermore, CA 94550, USA*

[d] *Center for Groundwater Research, Oregon Graduate Institute of Science and Technology, Portland, OR 97291-1000, USA*

Received 12 August 1998; accepted 21 December 1999

**Abstract**

Electrical imaging of tracer tests can provide valuable information on the spatial variability of solute transport processes. This concept was investigated by cross-borehole electrical imaging of a controlled release in an experimental tank. A saline tracer (conductivity $8 \times 10^3$ ms/m volume 270 l) was injected into a tank facility (dimensions $10 \times 10 \times 3$ m) consisting of alternating sand and clay layers. Injection was from 0.3 m below the surface, at a point where maximum interaction between tank structure and tracer transport was expected. Repeated imaging over a two-week period detected non-uniform tracer transport, partly caused by the sand/clay sequence. Tracer accumulation on two clay layers was observed and density-driven spill of tracer over a clay shelf was imaged. An additional unexpected flow pathway, probably caused by complications during array installation, was identified close to an electrode array. Pore water samples obtained following termination of electrical imaging generally supported the observed electrical response, although discrepancies arose when analysing the response of individual pixels. The pixels that make up the electrical images were interpreted as a large number of breakthrough curves. The shape of the pixel breakthrough-recession curve allowed some quantitative interpretation of solute travel time, as well as a qualitative assessment of spatial variability in advective-dispersive transport characteristics across the image plane. Although surface conduction effects associated with the clay layers complicated interpretation, the plotting of pixel breakthroughs was considered a useful step in the hydrological interpretation of the tracer test. The spatial coverage

* Corresponding author. Fax: +1-816-235-5535.

*E-mail addresses:* slaterl@umkc.edu (L. Slater), a.binley@lancaster.ac.uk (A.M. Binley), daily1@llnl.gov (W. Daily), rjohnson@ese.ogi.edu (R. Johnson).

[1] Formerly at Department of Environmental Science, Institute of Environmental and Natural Sciences, Lancaster, LA1 4YQ, UK.

[2] Fax: +44-1524-593985.

[3] Fax: +1-510-422-3013.

[4] Fax: +1-503-748-1273.



PII: S0926-9851(00)00002-1

provided by the high density of pixels is the factor that most encourages the approach. 

*Keywords:* Resistivity; Tomography; Solute transport; Pixel-breakthroughs

## 1. Introduction

An improved understanding of the mechanisms of ground water flow and solute transport is vital if the threat caused by man's pollution of the subsurface is to be comprehended and, hence, mitigated. In response to this threat, a significant component in the development of the environmental geophysics discipline has focused on the application of high resolution geophysical methods for the characterisation of flow and transport. As a result of these efforts, the concept of monitoring time variations in geophysical properties caused by fluid flow and solute transport arose. Applications include, as examples, (1) monitoring of tracer tests to infer groundwater flow rates and direction (White, 1988; Osiensky and Donaldson, 1995), (2) detection of leaks from pollutant containment facilities (Ramirez et al., 1996), (3) tracking leachates from landfills (Buselli et al., 1990), and (4) monitoring of seepage through earth dams (Butler and Llopis, 1990; Johansson and Dahlin, 1996). An analysis of recent environmental geophysics literature shows a continued evolution from the traditional investigation of time-static properties towards the investigation of such dynamic hydrological systems.

This application of geophysics is driven by the inherent disadvantages associated with the conventional methods for monitoring of hydrologic processes. Conventional methods typically require invasive sampling such that the natural flow regime may be disturbed. Financial and/or time constraints limit the number of sample locations. A high degree of interpolation between sample locations is then required to define a spatially continuous estimate of measured parameters. Sampled volumes are often small (typically centimetre scale) such that careful interpretation in terms of active larger scale hydrological processes is required. In contrast, the geophysical approach typically provides a non-invasive and indirect sampling approach, discrete measurements with a high sampling density and an opportunity to vary the measurement scale through appropriate survey design. This is particularly important given the recent rapid development of stochastic modelling techniques for groundwater flow and transport.

Methods that are sensitive to changes in the electrical properties of the ground are well suited to the monitoring of hydrologic processes. Electrical resistivity varies with solute concentration and degree of saturation and can be equated to these hydrological properties (Archie, 1942). Galvanic resistivity (White, 1994; Osiensky and Donaldson, 1995) and electromagnetic (Wilt et al., 1995) methods have both been applied to the monitoring of flow and solute transport. Dielectric properties are affected by the degree of saturation and solute chemistry such that ground penetrating radar (GPR) has also been adopted as a technique for hydrological monitoring (Brewster et al., 1995). Induced polarisation (IP) is strongly influenced by solute concentration yet relatively insensitive to the degree of saturation. Vanhala (1996) describes the application of IP to temporal monitoring of solute transport.

Recent advances in tomographic geophysical techniques have allowed high resolution imaging of changes caused by flow and solute transport (Daily et al., 1992, 1995). Tomography requires a large number of measurements to be made between transmitters and receivers placed at the surface or between boreholes, from which geophysical images of the system state at selected times can be obtained. The spacing selected between transmitters and receivers controls the scale and resolution. Electrical resistivity tomography (ERT) imaging of

solute infiltration through sand/clay layers was demonstrated by Daily et al. (1992). The locations of preferential flow pathways, as well as flow restrictions caused by clay layers, were inferred from temporal changes observed in the images. Electromagnetic tomography imaging of resistivity changes caused by injection of a saline tracer was performed by Wilt et al. (1995). Brewster et al. (1995) used GPR tomography to track the progress of a saline tracer through fractured bedrock.

In this paper, a controlled cross-borehole ERT experiment performed in a field-scale experimental tank during the summer of 1996 is documented. This experiment differs from previously published ERT investigations of flow and transport in that relatively good geological control was available and controlled tracer injection was performed. In addition, the use of a PC-operated multi-channel resistivity meter allowed a high temporal sampling density relative to previous experiments.

One objective of this paper is to explore the value of the analysis of image pixel breakthrough curves. Results of ERT investigations of flow and solute transport are typically presented as a sequence of resistivity (or conductivity) images or, more appropriately, resistivity (or conductivity) changes relative to some background condition. Such presentation gives the spatial distribution of a tracer at some time or indicates how a tracer has progressed between two times. Hydrological interpretation of a tracer test often involves an analysis of how a particular point in the system responds over time. Solute breakthrough curves are plotted and modelled to determine the advective-dispersive characteristics of the system at a particular point. Assuming a close correlation between fluid electrical conductivity and bulk electrical conductivity, the plotting of pixel breakthrough curves may therefore afford some interpretation of the subsurface advective-dispersive behaviour.

A second objective of this paper is to highlight the complications that arose with this tank experiment. Certain difficulties in interpretation arose as a result of (1) complications during the tank construction (filling with sand and clay layers), and (2) the chosen background hydrogeological condition prior to tracer injection. Although these complications did not prevent the primary objective of the paper from being achieved, they are highlighted here in order to assist workers involved in the design of similar hydrogeological experiments utilising electrical imaging.

## 2. Experimental tank facility

This tracer test was performed in a 10-$m^2$, 3-m deep experimental tank constructed at the Oregon Graduate Institute of Science and Technology, Portland, OR (Daily et al., 1998). The tank boundary is a double-walled plastic liner which confines released contaminants within the tank. Four electrode arrays, each consisting of 12 electrodes spaced at 0.25 m intervals, were installed prior to filling this tank. The electrodes were constructed from stainless steel mesh (Type 304 stainless) and mounted on insulating PVC pipe (0.5 in. diameter). Insulated copper wire was run up the inside of the pipe to make electrical contact between the electrodes and the resistivity instrument. Surface electrode arrays were not incorporated due to the poor electrical contact between the electrodes and the dry sand at the surface.

The tank was filled with dune sand from a nearby quarry with no effort towards layering or consolidation. Two layers of powdered bentonite were included, the planned tank structure being shown in Fig. 1. The location of electrodes is also shown. The top layer, located at a depth of 1.1 m, is approximately 0.07 m thick powdered bentonite and terminates to form a shelf at the centre of the electrode arrays. The lower layer was planned as two units; a 0.07 m powdered bentonite layer, located at 2.1 m, immediately beneath a 0.25 m mixture of 1% bentonite and sand. Emplacement of this struc-

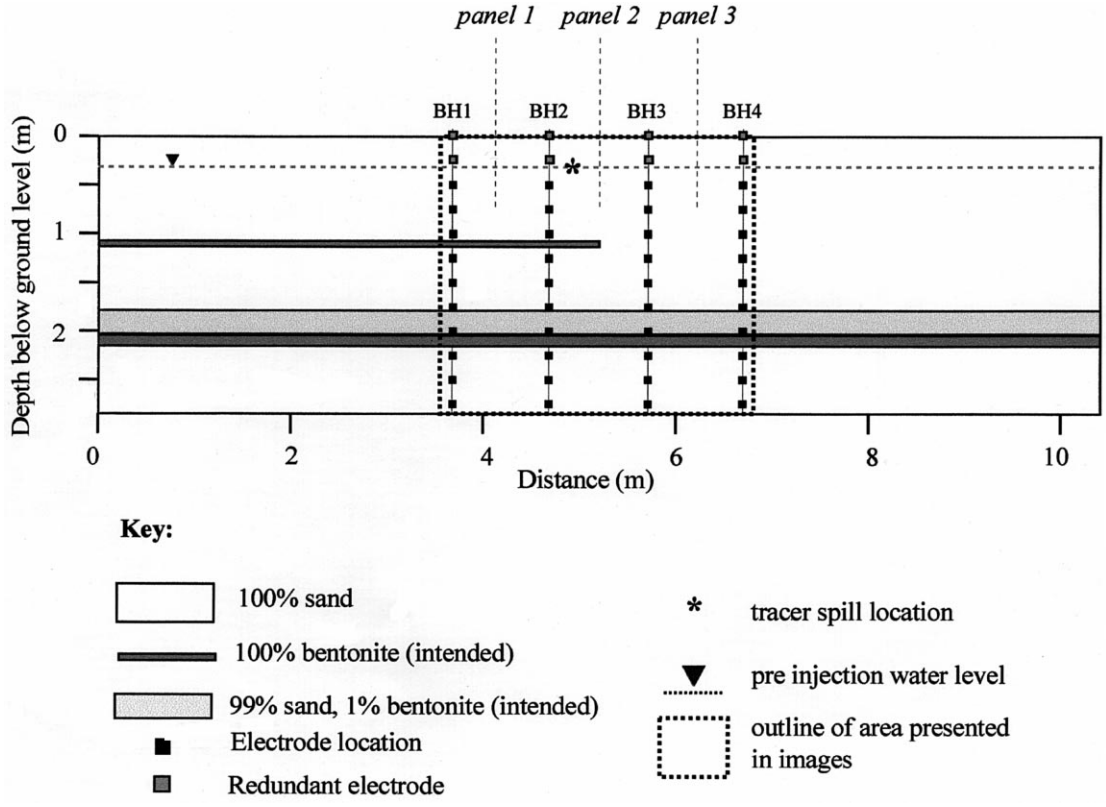


Fig. 1. Cross-section along image plane of intended experimental tank structure; expected deviations are discussed in the text.

ture was not entirely successful as it proved difficult to construct the bentonite/sand slurry on top of the powdered bentonite layer without mixing of the two. It is likely that the lower layer is a heterogeneous mixture of the slurry and the bentonite, about 0.3 m thick. In addition, some mixing with the sand above and below both bentonite layers was unavoidable during construction. Consequently, the 'sand' between clay layers must be considered to have some variability in terms of porosity, grain size and resistivity. Away from the clay layers (i.e., above 1.5 m in the region between BH3 and BH4) the sand is considered relatively homogeneous. The structure is laterally continuous (within the limits of the construction procedure) in the plane perpendicular to this cross-section (into the paper). Despite the complications with the tank construction, the structure is somewhat representative of an alternating sand/clay sedimentary sequence, in which non-uniform tracer transport can be expected.

The clay layers are high conductivity targets for ERT imaging. Laboratory measurements on sand similar to that placed in the tank gave the resistivity of the sand as 700 Ω m when saturated with tap water of conductivity 5.4 ms/m (formation factor = 3.8). The resistivity of bentonite slurry was 3 Ω m (average of three repeat measurements); this slurry was made by mixing bentonite powder with tap water (5.4 ms/m). The resistivity of the sand/bentonite mix was not measured but was expected to be significantly less than the pure sand as small amounts of clay provide surface conduction pathways that reduce bulk resistivity.

For the duration of this experiment the tank was kept in a near saturated state, the water level (measured in an observation well) prior to tracer injection being only 0.3 m below the tank

surface (Fig. 1). Significant rainfall events during the monitoring period (April 1st–April 12th 1996) were confined to an event on April 6th, 24 h prior to the termination of tracer injection, and an event on April 11th (24 h prior to the collection of the final dataset). As a result of heavy rainfall in the two months prior to this experiment (the 'Oregon floods', February 1996), the tank pore fluid was well flushed with clean water. As minimal electrical contrast between the water added by the two rainfall events and the pore water can be assumed, the primary complication to the data interpretation caused by these events was the increased saturation of the near surface sand. By the end of the experiment, the water level was only 0.14 m below the surface (a rise of 0.16 m). Given the porosity of the sand is 0.38, only 23% of this rise can be associated to the input tracer volume. Temperature variations during the monitoring period were moderate (45–65°F) and not considered to have significantly affected resistivity.

## 3. Tracer design

An order of magnitude estimate for the gravity induced flow of a parcel of fluid of density $\rho_o$ (kg $m^{-3}$) through a medium saturated with an otherwise stagnant fluid of density $\rho_\alpha$ (kg $m^{-3}$) is given by Falta et al. (1989) as,

$$V_d = \frac{kg}{\mu}(\rho_o - \rho_a) \quad (1)$$

where $V_d$ = Darcy velocity (m $s^{-1}$), $k$ = permeability ($m^2$), $g$ = magnitude of gravitational acceleration (9.8 m $s^{-2}$) and $\mu$ = fluid dynamic viscosity (0.001 kg $m^{-1}$ $s^{-1}$). From Eq. 1 a suitable density contrast between the dense tracer and in-situ pore water was calculated. The permeability of the sand was measured as $2 \times 10^{-11}$ $m^2$, representative of clean sand (Schon, 1996). From Eq. 1, a tracer of concentration 40 g $l^{-1}$ (density contrast 40 kg $m^{-3}$) results in a downward velocity ($V_d$) ≈ 0.7 m $day^{-1}$. This is an overestimate of the average Darcy velocity in the tank as the retarding effect of the clay layers is not considered. However, given the length of the monitoring period (two weeks), a maximum Darcy velocity of 0.7 m $day^{-1}$ was considered the correct order of magnitude. Hence, a tracer concentration of 40 g $l^{-1}$ (conductivity $8 \times 10^3$ ms/m) was adopted for this study. Pore water samples obtained following the termination of the experiment at locations away from the tank center showed in-situ fluid conductivity to be 5–8 ms/m (~ 3 orders of magnitude lower than the selected tracer conductivity). This high salinity tracer could represent industrial brine contamination such as that occurring from oil wells (Hoekstra, 1998) or serious seawater intrusion into fresh groundwater of coastal aquifers (Gondwe, 1991).

The tracer source (shown in Fig. 1) was located to encourage interaction between tracer transport and the known tank structure. A total of 270 of tracer was injected at a rate of 30 ml/min. The tracer was fed into a glass tube inserted so that supply was from a 'point' source

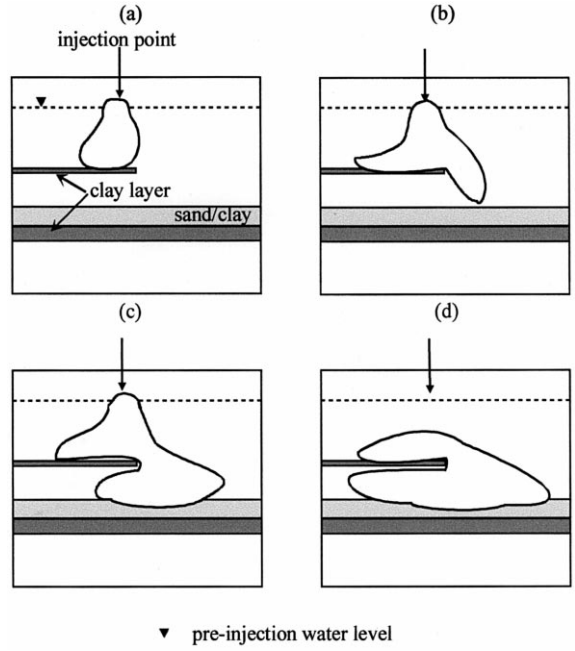


Fig. 2. Idealised plume evolution following tracer injection.

0.3 m below the surface, i.e., into the top of the saturated sediments (Fig. 1). Injection was continuous for 149 h. An idealised schematic of the expected plume evolution is given in Fig. 2.

## 4. Electrical imaging

As the ERT method is now well described in the geophysical literature (see for example LaBrecque et al., 1996) only a summary is provided here. Four electrode resistance measurements (the ratio of the voltage between an electrode pair to the current injected between another pair) are made for a large number of electrodes placed in boreholes or at the surface. Given these resistance measurements, it is possible to solve numerically for a single resistivity distribution that results in a set of calculated resistance measurements that best represent the measured response. The numerical solution applied here incorporates finite element forward modelling and minimisation of a weighted regularised objective function. Full details of the procedure are given in LaBrecque et al. (1996).

The spatial resolution of electrical imaging is not defined analytically as it is an unknown function of many factors including measurement error, electrode geometry, measurement schedule (number of independent measurements) and the resistivity distribution (Daily and Ramirez, 1995). During survey design, the spacing between electrodes will exert the fundamental control on resolution. Reducing the electrode spacing improves resolution but limits the investigated area, as current is focused in a smaller volume. Consequently, image resolution will decrease away from the electrodes due to the increased distance from the current source. The numerical modelling dictates that the best possible 'image resolution' is the size of one element of the finite element mesh. In order to examine the resolution of the final image of resistivity it is possible to determine the resolution matrix, as defined by Menke (1984).

The finite element mesh used in the resistivity modelling (LaBrecque et al., 1996) is shown in Fig. 3. The mesh is fine close to the electrodes (foreground region) with two elements per electrode separation. Towards the sides of

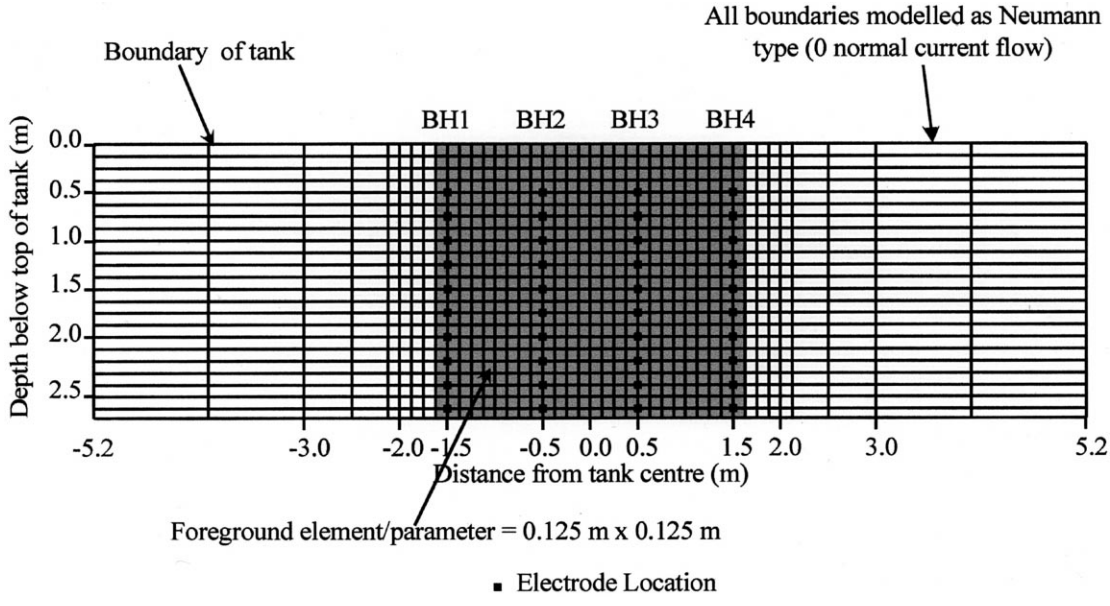


Fig. 3. Finite element mesh used in the modelling of resistivity structure for the experimental tank.

the tank the element width increases exponentially to reduce computational demand. The electrical insulation provided by the plastic liner was modelled as a Neumann-type boundary condition (current density perpendicular to the boundary is forced to zero). The modelling applied here assumes a 2-D resistivity distribution. The finite width of the tank in the plane perpendicular to the image plane violates this assumption. Due to the distance of the electrodes from the boundaries of this perpendicular plane (5 m as compared to 1 m between electrode arrays) the modelling errors should be small and acceptable given the objectives of this experiment. Numerical methods for imaging 3-D resistivity structure have been developed (for example, Loke and Barker, 1996). However, 3-D imaging requires time-consuming acquisition of very large datasets such that its application to imaging of tracer tests is currently limited. With future improvements in electrical imaging hardware, fast 3-D imaging of tracer tests is likely to be realised. This should significantly increase the value of electrical imaging as geological structure as tracer transport can rarely be two-dimensional.

## 5. Electrical measurements and noise characterisation

Definition of the 'best' measurement schedule (a list of four-electrode configurations to be addressed by the resistivity meter) remains a poorly resolved problem (LaBrecque, 1996, pers. comm.). A finite number of independent measurements $D$ can be related to the number of electrodes $N$,

$$D_4 = \frac{N(N-3)}{2} \quad (2)$$

for a four-electrode (dipole–dipole) dataset (Xu and Noel, 1993). Circulating measurement schemes have been recommended to guarantee completeness of an ERT dataset (Xu and Noel, 1993).

The circulating dipole–dipole schedule ('nearest neighbour schedule'), as shown in Fig. 4a, has been used in the medical field (Thomas et al., 1991) and for imaging of soil cores (Binley et al., 1996). Current is injected between two adjacent electrodes and potentials are measured between all remaining adjacent electrode pairs. The current electrodes then circulate by one electrode and all potential pairs are again recorded. One problem with this schedule is that current flow is biased towards the near-borehole region such that resolution at the centre is poor. In addition, the small distance between potential electrodes results in a small voltage signal and a low signal-to-noise ratio (SNR). To offset this problem, circulating dipole 'skip one' and 'skip two' measurement schedules were devised (Fig. 4a). The greater distance between current electrodes improves resolution away from the boreholes (as confirmed by synthetic modelling) and the increased distance between voltage electrodes improves the SNR. Both 'skip one' and 'skip two' schedules were used to compensate for the loss of some of the independent measurements; the circulating dipole schedule contains 170 measurements for two boreholes with 10 electrodes each (Eq. 2, using $N = 20$) whereas the 'skip one' and 'skip two' contain only 110 measurements each. Consequently, each between-borehole dataset contained 220 measurements.

Accurate quantification of measurement errors (noise) is crucial to prevent misinterpretation of ERT images (LaBrecque et al., 1996). Measurement noise limits resolution of electrical structure. Incorrect noise estimation can result in gross smoothing of structure (noise overestimation) or artificial image structure (noise underestimation). Noise can arise from such factors as (1) poor electrode contact causing systematic errors associated with a particular electrode, (2) random errors associated with the measurement device, and (3) sporadic errors related to external factors (background noise).

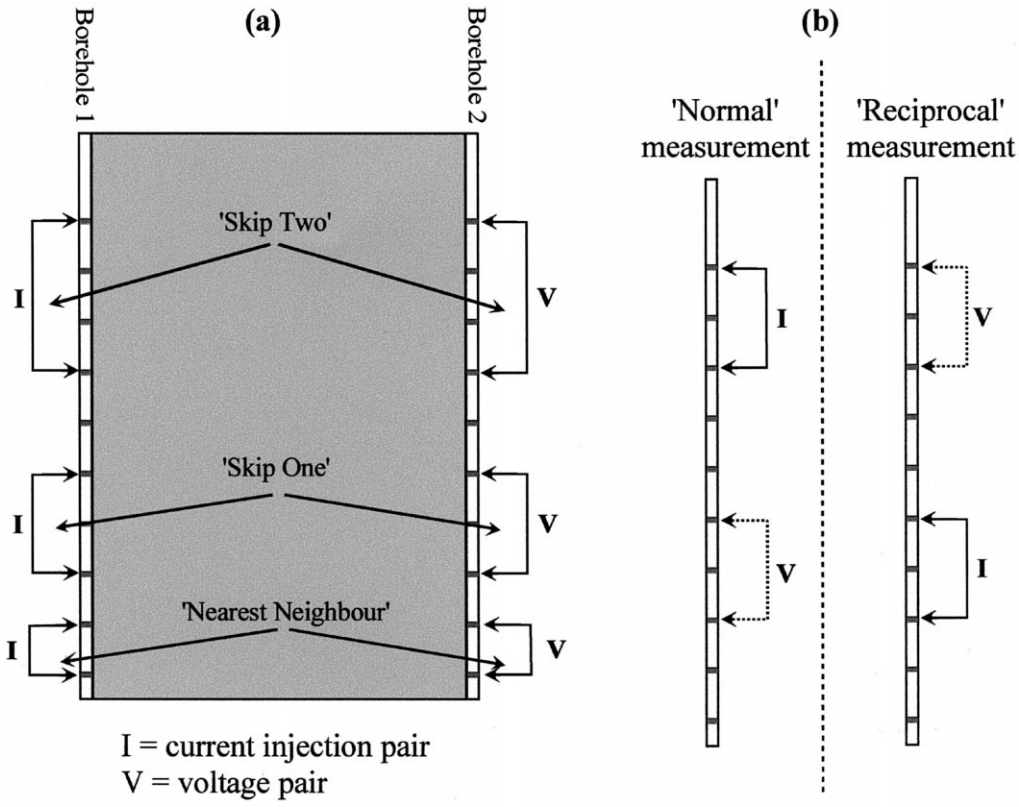


Fig. 4. (a) Circulating measurement configurations used in electrical imaging. (b) The ‘‘normal’’ transfer resistance measurement and its reciprocal.

Repeatability tests (stacking) are an obvious measure of noise quantification. An alternative measure is the ‘reciprocal error’, defined as,

$$e = R_n - R_r \quad (3)$$

where $R_n$ is the ‘normal’ resistance measurement and $R_r$ is the ‘reciprocal’ resistance measurement (Fig. 4b). As exchanging the current electrodes with the potential electrodes should not affect the measured resistivity (principle of reciprocity), $e$ is a measure of data noise. The reciprocal error can detect errors that may not be apparent from repeatability checks. One example is the case of bad earth contact at a voltage electrode; the potential between the one connected voltage electrode and the ground on the instrument may be recorded. Interchanging the potential and current electrodes would identify this problem. In this experiment, both repeatability errors and reciprocal errors were quantified for each measurement.

The reciprocal errors were used to identify bad measurements and to quantify error parameters for the inversion. The inversion uses a simple Gaussian error model in which the magnitude of reciprocal error $|e|$ increases with the magnitude of measured resistance $|R|$ according to,

$$|e| = a + b|R| \quad (4)$$

Parameter $a$ defines the minimum error whereas parameter $b$ defines the increase in $|e|$ with $|R|$. Plots of the reciprocal error against resistance for the background dataset are shown in Fig. 5. After removal of obvious outliers (typically $|e| > 10\%$ of $|R|$), the error parameters are defined by an envelope that encompasses all remaining measurements.

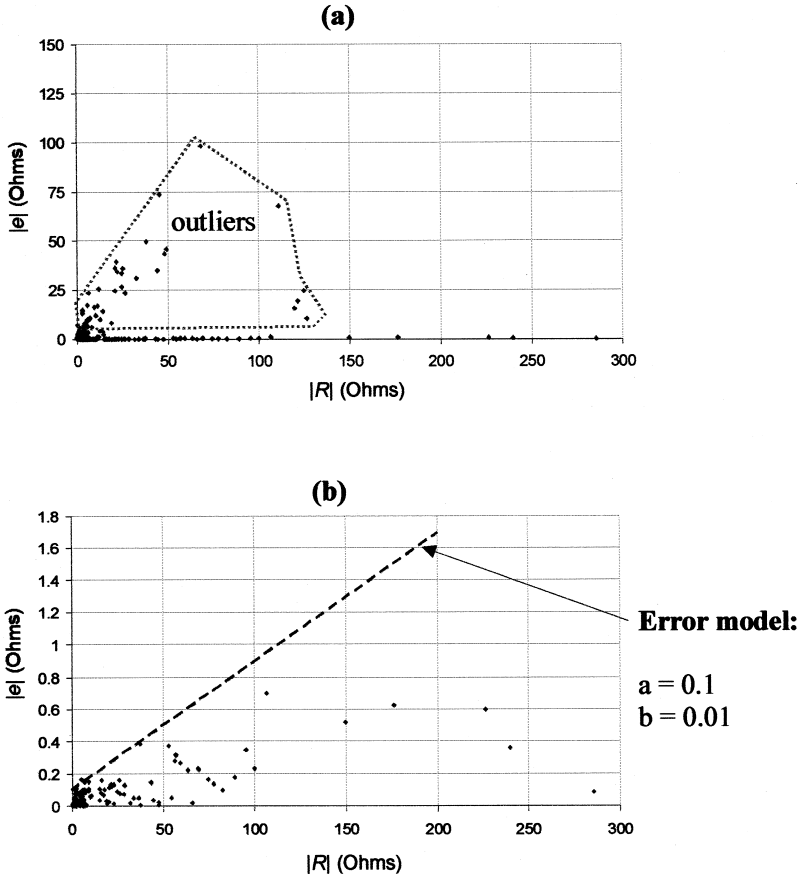


Fig. 5. (a) Magnitude of reciprocal error $|e|$ plotted against magnitude of transfer resistance $|R|$ for all measurements in the background dataset prior to tracer injection. (b) Remaining errors after removal of obvious outliers; the envelope defines the parameters of the error model.

Electrical measurements were made between boreholes 1–2 (Panel 1), 2–3 (Panel 2) and 3–4 (Panel 3) using the lowermost 10 electrodes of each borehole (Fig. 1) as the resistive unsaturated sand prevented reliable data acquisition using the two uppermost electrodes of each array. A 15-channel data acquisition system (Zonge GDP32), capable of addressing up to 30 electrodes, was employed. This allowed a complete three-panel dataset (1320 measurements, including the 660 reciprocals) to be collected in approximately 45 min. ERT monitoring of dynamic hydrological systems requires geophysical equipment that can provide such high data acquisition rates. Prior to tracer injection, a reference 'background' dataset was obtained. During the first day of tracer injection, measurements were continually made as fast as the data acquisition hardware would allow. In the following period up to two weeks after tracer injection, datasets were collected at least twice daily. Assuming the transport rate to be $\approx 0.7$ m day$^{-1}$, each image represents a 'snap-shot' depiction of the tracer evolution at a particular time.

## 6. Electrical images

The resistivity image obtained prior to tracer injection ('background') is shown in Fig. 6. As expected, two horizontal low resistivity bands correlate with the clay layers. However, the true layer resistivity (3 Ω m) and thickness (0.07 m)

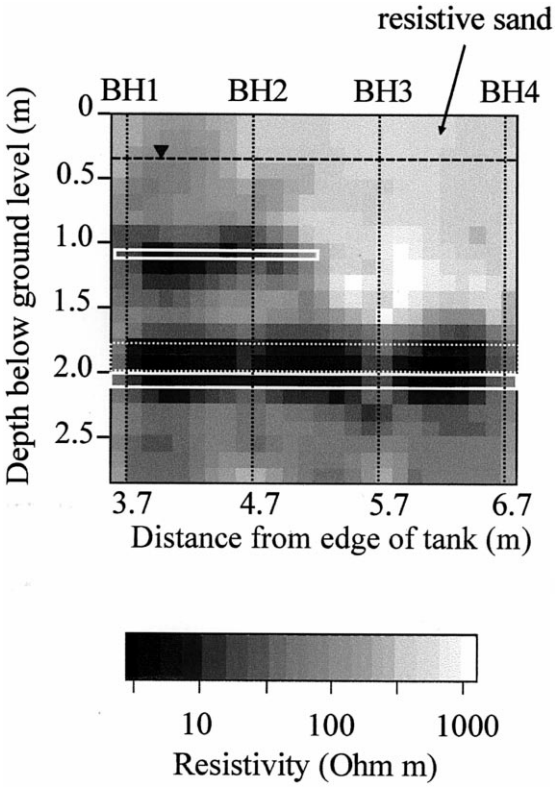


Fig. 6. Resistivity structure obtained from inversion of electrical measurements prior to tracer injection (background dataset).

are not resolved as the maximum resolution (0.125 m as defined by the size of the finite elements) is insufficient to resolve this fine structure. In addition, the smoothness constrained inversion results in a transitional resistivity structure in which layer interfaces are not well defined. Consequently, the inversion fits an equivalent layer, which satisfies the data; both the thickness ($\sim$0.38 m) and the resistivity (6–18 $\Omega$ m) of this equivalent layer are overestimates of the true structure. The thickness of the lower layer (powdered bentonite and slurry layers combined) is resolved as a $\sim$0.38 m thick layer in the image; this compares well with the estimated 0.3 m true layer thickness. The resistivity of this lower layer is 5–16 $\Omega$ m; the true resistivity of this layer is not known, but is likely variable due to the mixing between the powdered bentonite and slurry that occurred during construction. The lowest resistivities probably represent zones of undisturbed bentonite.

Only when away from the sand layers (upper right corner of image) does the imaged resistivity climb to 1000 $\Omega$ m, comparable with the 800 $\Omega$ m measured for the tap water saturated sand sample in the laboratory. The higher in-situ values probably arise as a result of the flushing of the near surface sand with clean rainwater during February 1996 ('Oregon floods'). Beneath the lower clay layer and between the upper and lower layers, the resistivity is only 100–200 $\Omega$ m, a result of the unavoidable mixing of the sand with the bentonite that occurred during array installation. The water table is not resolved in this image. This is primarily due to the reduced resolution near the tank surface, as evident from the diagonal of the

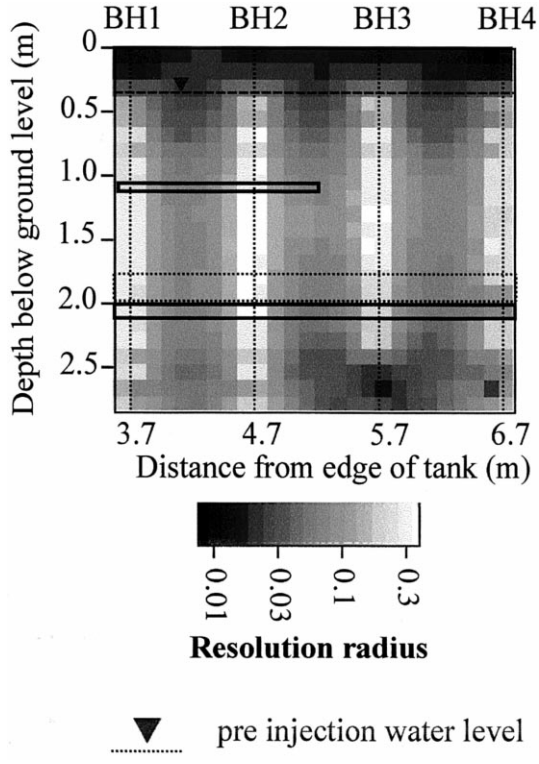


Fig. 7. Resolution matrix for the dataset collected prior to tracer injection (background dataset). Values of the resolution matrix range from zero to unity, by definition with lower values indicating poorer resolution.

resolution matrix for the three borehole–borehole planes (Fig. 7). Values of the resolution matrix range from zero to unity, by definition. Values close to unity indicate perfect resolution, lower values reveal areas of poorer resolution. The poor resolution above 0.5 m arises as the

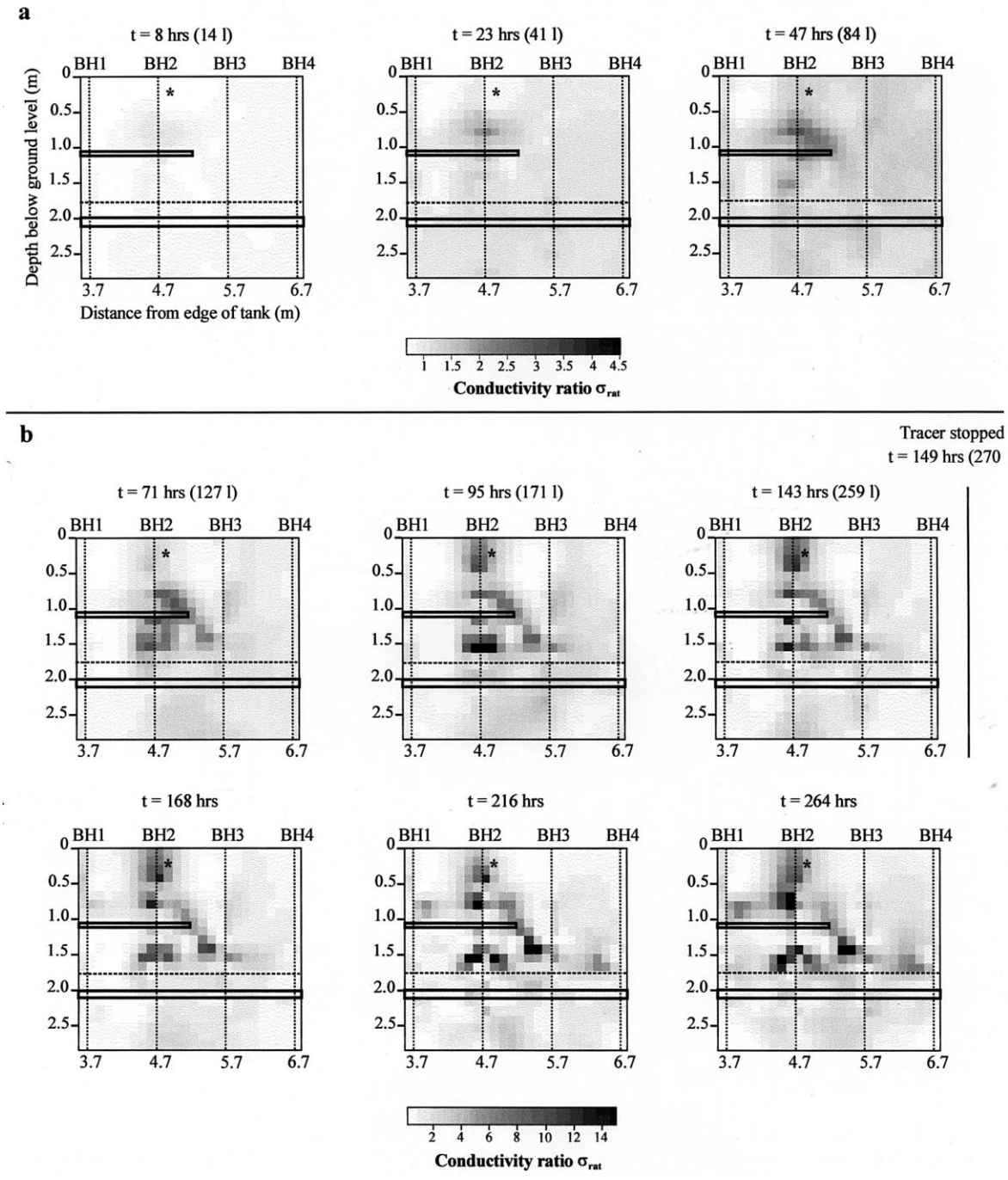


Fig. 8. Images of conductivity ratio at nine times during tracer injection. (a) Between 8 and 47 h after the start of the tracer injection. (b) Between 71 and 264 h after the start of the tracer injection.

first measuring electrode is at 0.5 m, such that the current density in the top 0.5 m is low relative to below 0.5 m. Fig. 5 also shows that, as expected, resolution is greatest close to the boreholes. A second factor preventing the detection of the water table may be the low electrical contrast between fresh-water ($\sim 5$ ms/m) saturated, and unsaturated, clean sand.

ERT imaging of tracer transport is best presented using images of conductivity change relative to the pre-tracer condition. Conductivity structure caused by time-static features, such as the sand-clay sequence, is then not apparent in the image, thereby enhancing visualisation of the time varying features. Assuming other factors that affect conductivity (porosity, saturation and temperature) remain constant, images of conductivity change reflect tracer migration alone. In the presentation of image changes, one approach is simply to subtract the pixel conductivity at time $t$ after tracer injection from the pre-injection value. However, as errors are additive when taking the difference of two numbers, the resulting images can be noisy. An alternative is to perform the modelling and inversion on a conductance ratio $C_{rat}$ between two datasets defined as,

$$C_{rat} = \frac{C_t}{C_O} C_F \quad (5)$$

where $C_t$ is a conductance measurement at time $t$, $C_O$ is the pre-injection conductance measurement and $C_F$ is the theoretical conductance for an arbitrary homogeneous conductivity distribution. The output is an image of relative conductivity (conductivity ratio) $\sigma_{rat}$, in which a value of 1 indicates no change between datasets (Daily and Owen, 1991). Values of $\sigma_{rat}$ greater than 1 indicate zones of conductivity increase whereas values less than 1 indicate conductivity decrease. In addition to preventing error propagation, application of Eq. 5 is advantageous as the scaling by $C_F$ reduces the complicating effect of departures from a 2-D conductivity distribution, as detailed in Ramirez et al. (1996).

Images of conductivity ratio at nine times after tracer injection are shown in Fig. 8. In order to enhance the subtle changes that occur in the early stages of injection, the first three images are plotted on a separate scale. The overall picture of tracer transport is as follows: after 23 h accumulation upon the upper clay layer is observed. Transport over the edge of the clay layer is suggested after 47 h and well defined after 95 h. Spreading along both the upper and lower clay layer is apparent after 143 h and somewhat enhanced in the final three datasets. These images are consistent with the order of magnitude prediction of vertical plume transport of 0.7 m/day, as after $t = 23$ h saline water is imaged at 1.0 m. The upper clay layer impedes further vertical transport at this point.

After 71 h, the image indicates evidence for a transport pathway not expected from the layering and the assumed plume evolution (Fig. 2). High $\sigma_{rat}$ values are apparent immediately above the lower clay/slurry layer between about 4.5 and 5.0 m (see also $t = 95$ h). It is likely that, either damage to the upper clay layer occurred in this vicinity, or BH2 acted as a hydraulically conductive flow pathway through the upper layer. The effect of boreholes on subsurface flow structure is a limitation of ERT imaging (as with any method that involves invasion of the subsurface). Conductivity increases immediately above the tracer injection point may represent a localised increase in the groundwater level, although saturation was never observed at the surface. However, as discussed, the sensitivity in the top 0.5 m is poor such that observed changes in this zone are of questionable interpretation. Further discussion of the significance of the observed electrical changes is presented following the discussion of the concept of pixel breakthroughs.

## 7. Analysis of pixel breakthroughs

In applying electrical imaging to the interpretation of tracer tests, it seems reasonable to

attempt to present/interpret the data in a manner akin to established hydrological methods. ERT images are composed of a large number of pixels that are the elements of the finite element mesh. In this case, each element in the foreground region of Fig. 8 is a pixel in the image. Each pixel has a value $P$ that is the ratio of pixel conductivity at time $t$ to initial conductivity (Eq. 5). Binley et al. (1996) demonstrated how each pixel in a time sequence of electrical images obtained on laboratory soil cores could be interpreted as a 'breakthrough curve' of relative tracer concentration. This interpretation assumed (1) full saturation of the pore space, (2) changes in electrical conductivity are only due to changes in fluid conductivity, (3) electrical conductivity is linearly related to salt concentration, and (4) matrix conductivity is small relative to electrolytic conductivity.

In this study, assumptions 1 to 3 can be made if the analysis is performed excluding the upper 0.3 m of unsaturated sand. However, two bentonite layers, combined with the relatively low fluid conductivity prior to tracer injection (5–8 ms/m), violate the fourth assumption. In locations close to the bentonite, the relationship between fluid and pixel conductivity is influenced by the clay content. However, away from the bentonite this relationship will be relatively constant across the tank. Despite this complication caused by the surface conductance close to the bentonite, pixel breakthrough curves of ratio conductivity (translation to relative fluid conductivity not justified) should still provide a

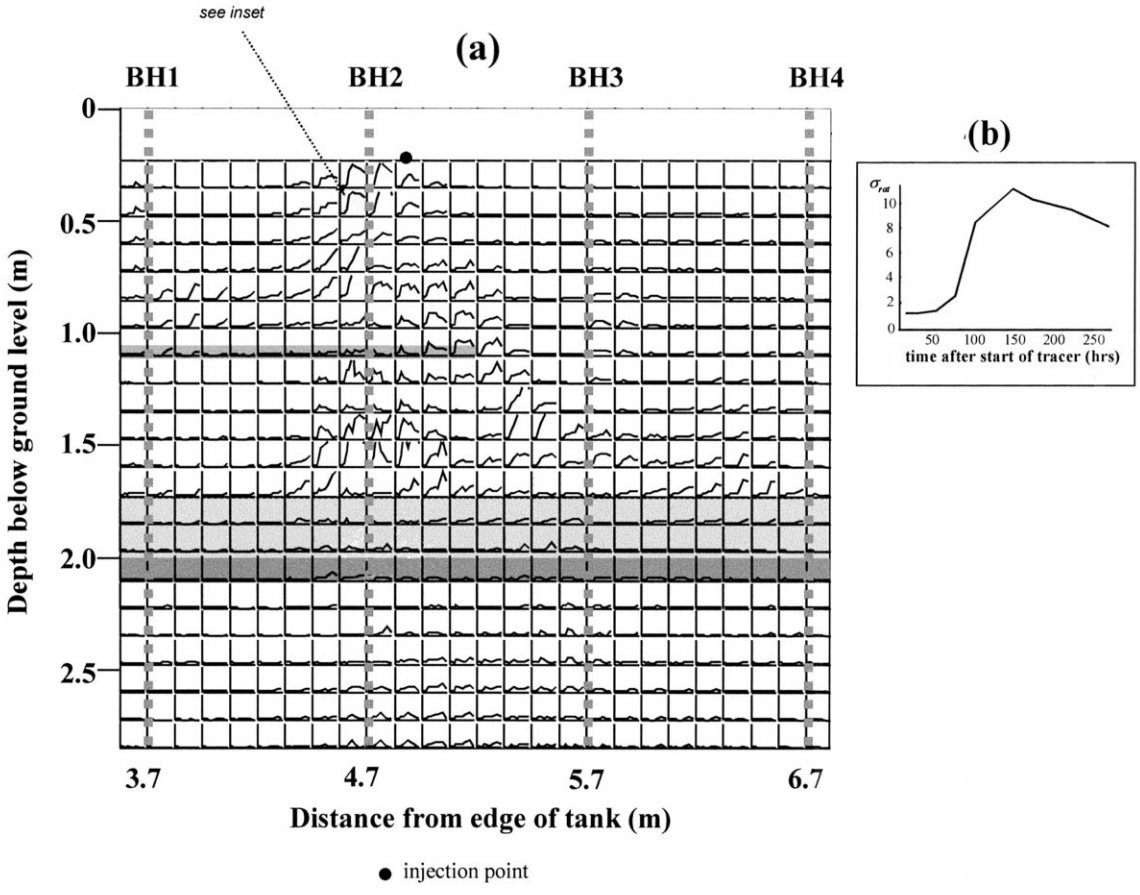


Fig. 9. (a) Pixel breakthrough response to tracer injection. (b) Example pixel showing scaling on time and conductivity ratio axes. A value of $\sigma_{rat} = 1$ indicates no conductivity change between datasets.

qualitative sense of variability in tracer transport characteristics (breakthrough-recession behaviour) within the tank.

Pixel 'breakthroughs' for all elements of the finite element mesh are shown in Fig. 9. Spatial variability in tracer breakthrough-recession behaviour is apparent and some correspondence with traditional advective-dispersive transport behaviour is observed. Early breakthrough times down to 1.7 m are observed in pixels adjacent to BH2, giving a clear indication of an unwanted hydraulic pathway through the upper clay layer. Early breakthrough times are also clearly associated with the desired flow pathway over the upper clay layer. The lack of pixel response at between 4.9–5.1 m and 1.25–1.5 m depth testifies to the separation of these two pathways. Pixel response along the top of the upper and lower layers is somewhat consistent with continued plume spreading along these layers.

Fig. 9 also reveals evidence for transport through the lower clay/slurry layer as significant breakthrough responses are observed beneath 2.2 m, particularly between BH2 and BH3. Difficulties encountered with the array installation resulted in structural heterogeneity in this layer. Although this could provide vertical preferential flow paths, tracer transport along BH2, and perhaps BH3, must also be expected. These pixel responses are not easily defined from the images of conductivity change (Fig. 8).

Pixels coincident with the low resistivity response to the clay layers (Fig. 6) show a damped breakthrough relative to breakthroughs observed within the sand. This may in part relate to minimal tracer invasion into the clay containing zone (both the clay layer and the surrounding sand that was partly mixed with clay during tank construction). However, as discussed, the fluid conductivity–bulk conductivity relationship is altered close to the layers as a result of the parallel surface conduction associated with the clay. This is likely the cause of the damped response in some of the pixels immediately above the upper and lower clay layers. Quantitative interpretation of the shape of pixel breakthroughs is, hence, complicated. However, the determination of first arrival time seems feasible as picking the first significant increase in conductivity is possible from both the sharp response observed in the sand and the damped response close to the clay. An image of time to first breakthrough is presented in Fig. 10. Such an image perhaps has greater meaning in terms of hydrogeology, relative to an image of conductivity change. The image is a rather crude representation of travel time as the sampling interval is coarse, particularly during the later stages of the experiment. However, the image concisely illustrates the two preferential flow pathways identified above.

In-situ pore fluid conductivity was sampled at discrete points following termination of the tracer experiment on April 12th 1996. Sampled conductivity varied from 5 ms/m (the pre-injection value in the sand) to $6 \times 10^3$ ms/m (tracer conductivity $= 8 \times 10^3$ ms/m). Sample locations (five wells) are superimposed on the image of conductivity ratio for the same day (Fig. 11), with values grouped into four categories for ease of presentation. In a general sense, the

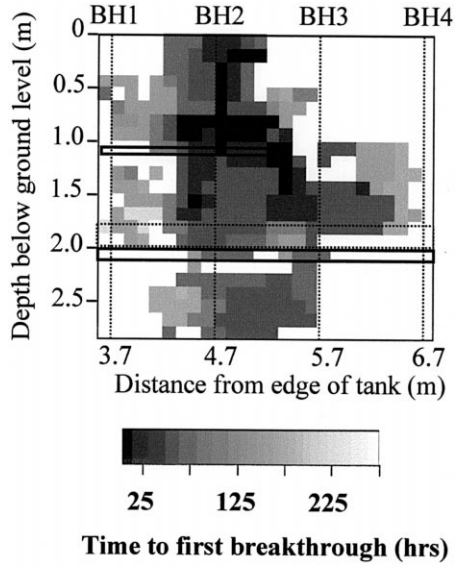


Fig. 10. Image of time to first tracer breakthrough for each pixel.

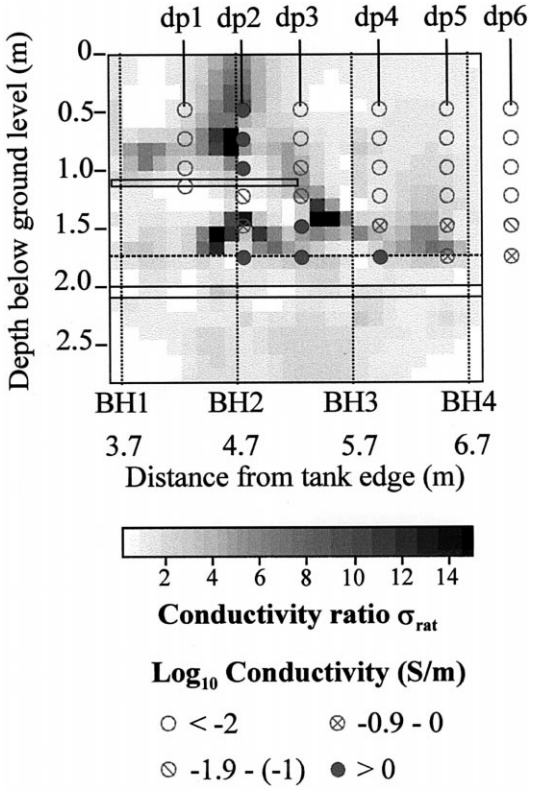


Fig. 11. Sampled fluid conductivity compared to modelled conductivity ratio at 48 locations; well dp6 is shown to illustrate conductivity away from boreholes and tracer.

samples support the distribution of conductivity change obtained from the imaging. Fluid conductivity is greatest along the top of the lower clay layer and close to BH2. The location of dp2 was selected to confirm the unwanted flow pathway through the upper clay layer, probably provided by BH2. High fluid conductivity is indeed observed along the length of dp2. For dp4 and dp5, the image pixel values are consistent with the samples of fluid conductivity; excluding the lower two samples, pre-injection values of fluid conductivity correlate with pixels showing no conductivity increase. Increased fluid conductivity at the fifth and sixth sample locations for dp6 indicates that tracer transport along the lower clay layer continued outside of the imaged plane.

Closer examination of image pixels at the sample locations reveals some discrepancies. Considering dp2, the first, second, fourth and fifth (from top) samples correlate well with sampled fluid conductivity; ratio conductivity is high where sampled fluid conductivity is high, and low where sampled fluid conductivity is low. However, the pixels at the third and sixth sample points correlate poorly with the high fluid conductivity at these locations. This might be the result of the effect of the parallel surface conduction pathway in the presence of high clay content. In such locations, large increases in fluid conductivity may not drastically increase bulk conductivity (relative to the increase that would be observed in clean sand). A similar lack of correlation between high fluid conductivity and pixel response is observed for the sixth sample in dp4. Along dp1 fluid conductivity samples do not support the elevated conductivity resolved in the pixels above the upper clay layer. However, ratio conductivity is generally lower in a strip centred on dp1, relative to either side.

The observed discrepancies likely in part reflect the non-unique nature of electrical resistivity imaging. The result from an inversion based on linear least-squares fitting of the data and model roughness is just one of a host of possible image solutions (the equivalence problem). In 2-D cross-borehole electrical imaging, the equivalence problem generally does not impede interpretation of overall image structure. However, when performing a detailed analysis of the magnitude of individual pixels, the non-unique nature of the image must always be considered.

## 8. Discussion

The hydrogeological interpretation of this controlled tracer test identifies the potential value of electrical imaging in groundwater studies. It seems reasonable to consider the image as a set of ‘samplers’ (pixels) which allow spatial analysis of (1) the distribution of travel times; and perhaps, (2) the degree to which advective, dispersive or combined advective-dispersive

transport occurs. The fundamental value is the very high 'sampler' density (598 pixels in this case), relative to that typically obtained with direct, invasive temporal monitoring of fluid conductivity. It is possible that such pixel breakthroughs could be applied to formulate a statistical characterisation of variability in transport parameters (e.g., advective velocity, dispersion coefficient). Such data could be utilised to constrain stochastically driven solute transport models.

However, the limitations of the method must be recognised. In this particular case, surface conduction effects associated with the two clay layers complicated spatial pixel correlation across the image. As a consequence, the only quantitative interpretation of the pixel breakthrough curves attempted here was the determination of first arrival times. The second limitation, fundamental to any electrical imaging survey, is the non-unique nature of the image solution. Non-uniqueness must be addressed when considering the hydrogeological significance of changes in individual pixels. Furthermore, pixel breakthrough curves are only useful to the extent that the imaging is reliable. This highlights the importance of careful error analysis and the removal of bad data prior to inversion. Thorough error analysis places additional demands on data acquisition.

The hydrogeological significance of pixel breakthroughs would have been better assessed if fluid conductivity could have been sampled at discrete points during the experiment. Although this was considered, concerns regarding disruption of the 'natural' subsurface flow by repeated invasive sampling prevented this approach. Permanent installation of fluid conductivity sensors prior to electrical imaging would improve future electrical imaging of tracer tests.

As a consequence of the indirect nature of the electrical measurement of fluid conductivity, hydrological interpretation following electrical imaging of a tracer test will be predominantly qualitative. However, for tests in the saturated zone it may be possible to quantify pixel solute concentration breakthroughs when surface conduction effects are negligible. This will arise when clay content is insignificant and/or fluid conductivity is sufficiently high that electrolytic conduction dominates. Quantitative modelling in terms of advective-dispersive parameters might then be appropriate. However, this condition is not frequently met in the field. The primary hydrological value of electrical imaging is, hence, considered to be the improved spatial coverage of qualitative information that can be related to variations in transport characteristics. Efficient quantification of transport characteristics at a study site could follow from focusing of direct hydrological measurements/sampling based on transport-induced changes observed in the electrical images. In this manner, a relatively small number of direct measurements/samples might quantify the primary transport properties at a study site.

Certain problems with interpretation arose as a result of ERT experimental design. The hydraulic heterogeneity within the tank significantly differed from that intended (Fig. 1). Swelling of the bentonite upon saturation undoubtedly caused some mixing between sand and clay. As the nature of this mixing could not be quantified, it reduced the level of control on the tank conditions. The major cause of problems encountered during ERT installation appears to have been a preferential flow pathway close to BH2. The sampled post-experiment fluid distribution supports this conclusion. It is likely that the electrode array itself contributed to the hydraulic conductivity of this flow path. The disruption of the natural flow regime by the emplacement of electrode arrays is a problem general to cross-borehole electrical imaging. Care should be taken to avoid/minimise the hydraulic connections caused by the borehole. In this case, the relatively close proximity of the tracer injection point to BH2 may have encouraged tracer transport along this borehole. In addition, the electrical imaging indicates some tracer transport through the lower clay layer (again possibly via electrode arrays). On a posi-

tive note, this example illustrates how electrical imaging is capable of defining relatively complex flow pathways (including unexpected ones) in layered media.

A second problem with the ERT experiment design relates to the unsaturated state of the upper 0.4 m prior to tracer injection. As a result of the high contact resistance between electrode and dry sand, the top two electrodes (at 0 and 0.25 m) were rendered redundant. The result was poor image resolution in the upper 0.5 m, as revealed by the resolution radius (Fig. 7). Consequently, the location of the water level was not resolved in the imaging, except close to the tracer injection after 95 h of tracer input. Two rainfall events during the period of imaging increased the water level but probably had little effect on the fluid conductivity distribution, due to the similar conductivity of the rain water and in-situ tank fluid.

## 9. Conclusions

In an experimental tank, tracer migration through a synthetic alternating sand/clay sequence was observed. Images revealed preferential flow through the sand and retardation at the clay layers. Analysis of the 598 pixel breakthroughs offered the opportunity to examine the spatial variation in the time-response to tracer transport in a conventional hydrological sense. A crude quantitative assessment of travel times and a qualitative overview of advective-dispersive transport characteristics were obtained from the breakthrough curves. Unexpected vertical flow paths caused by complications with array installation were identified and supported by post-imaging sampling of fluid conductivity at discrete points within the tank. In particular, natural gravity induced flow was disturbed by the presence of a carefully installed borehole, illustrating how invasive drilling can affect aquifer hydraulic properties.

In this study, tracer transport was modelled in two dimensions: as hydrological processes are inherently three dimensional, such two-dimensional characterisation is not ideal. Computational advances have made three-dimensional electrical imaging possible. New resistivity imaging systems are being marketed that offer rapid data acquisition rates. These systems are ideal for monitoring tracer tests using permanent electrode installations. Given continued advances in these two areas, improved resolution of tracer transport from electrical imaging may be anticipated.

## Acknowledgements

This work was supported by Ph.D. studentship GT4/94/171/L (Natural Environment Research Council) awarded to the first author. Special thanks are owed to Matt Perrot (Center for Groundwater Research, Oregon Graduate Institute of Science and Technology) for assistance with fieldwork.

## References

Archie, G.E., 1942. The electrical resistivity log as an aid in determining some reservoir characteristics. Trans. Am. Inst. Min. Metall. Pet. Eng. 146, 54–62.

Binley, A., Henry-Poulter, S., Shaw, B., 1996. Examination of solute transport in an undisturbed soil column using electrical resistance tomography. Water Resour. Res. 32, 763–769.

Brewster, M.L., Annan, A.P., Greenhouse, J.P., Kueper, B.H., Olhoeft, G.R., Redman, J.D., Sander, K.A., 1995. Observed migration of a controlled DNAPL release by geophysical methods. Ground Water 33, 977–987.

Buselli, G., Barber, C., Davis, G.B., Salama, R.B., 1990. Detection of groundwater contamination near waste disposal sites with transient electromagnetic and electrical methods. In: Ward, S.H. (Ed.), Investigations in Geophysics No. 5: Geotechnical and Environmental Geophysics. Environmental and Groundwater Vol. 2 Society of Exploration Geophysicists, Oklahoma, pp. 27–39.

Butler, D.K., Llopis, J.L., 1990. Assessment of anomalous seepage conditions. In: Ward, S.H. (Ed.), Investigations in Geophysics No. 5: Geotechnical and Environmental Geophysics. Environmental and Groundwater Vol. 2 Society of Exploration Geophysicists, Oklahoma, pp. 153–173.

Daily, W., Owen, E., 1991. Cross-borehole resistivity tomography. Geophysics 56, 1228–1235.

Daily, W., Ramirez, A., Johnson, R., 1998. Electrical impedance tomography of a perchloroethylene release. J. Environ. Eng. Geophys. 2 (3), 189–202.

Daily, W., Ramirez, A., LaBrecque, D., Barber, W., 1995. Electrical resistance tomography experiments at the Oregon Graduate Institute. J. Appl. Geophys. 33, 227–237.

Daily, W., Ramirez, A., LaBrecque, D., Nitao, J., 1992. Electrical resistivity tomography of vadose water movement. Water Resour. Res. 28, 1429–1442.

Gondwe, E., 1991. Saline water intrusion in southeast Tanzania. Geoexploration 27, 25–34.

Hoekstra, P., 1998. Geophysical surveys for mapping brine contamination resulting from oil and gas production. In: Symposium on the Application of Geophysics to Engineering and Environmental Problems (SAGEEP), March 22–26, Chicago, IL. pp. 197–204.

Johansson, S., Dahlin, T., 1996. Seepage monitoring in an earth embankment dam by repeated resistivity measurements. Eur. J. Environ. Eng. Geophys. 1, 229–247.

LaBrecque, D.J., Miletto, M., Daily, W., Ramirez, A., Owen, E., 1996. The effects of noise on Occam's inversion of resistivity tomography data. Geophysics 61, 538–548.

Loke, M.H., Barker, R.D., 1996. Practical techniques for 3D resistivity surveys and data inversion. Geophys. Prospect. 44, 499–523.

Menke, W., 1984. Geophysical Data Analysis: Discrete Inverse Theory. Academic Press.

Osiensky, J.L., Donaldson, P.R., 1995. Electrical flow through an aquifer for contaminant source leak detection and delineation of plume evolution. J. Hydrol. 169, 243–263.

Ramirez, A., Daily, W., Binley, A.M., LaBrecque, A., Roelant, D., 1996. Detection of leaks in underground storage tanks using electrical resistance methods. J. Environ. Eng. Geophys. 1, 189–203.

Schon, J.H., 1996. Physical properties of rocks: fundamentals and principles of petrophysics, Handbook of Geophysical Exploration; Seismic Exploration. Pergamon.

Thomas, D.C., McArdle, F.J., Rogers, V.E., Beard, R.W., Brown, B.H., 1991. Local blood volume changes in women with pelvic congestion measured by applied potential tomography. Clin. Sci. 81 (3), 401–404.

Vanhala, H., 1996. Monitoring the integrity of liner construction using induced polarisation. In: Proceedings of the Symposium on the Application of Geophysics to Environmental and Engineering Problems, April 28th–May 2nd, 1996, Keystone, CO. pp. 1017–1026.

White, P.A., 1988. Measurement of ground-water parameters using salt-water injection and surface resistivity. Ground Water 26, 179–186.

White, P.A., 1994. Electrode arrays for measuring groundwater flow direction and velocity. Geophysics 59, 192–201.

Wilt, M.J., Alumbaugh, D.L., Morrison, H.F., Becker, A., Lee, K.H., Deszcz-pan, M., 1995. Crosswell electromagnetic tomography: system design considerations and field results. Geophysics 60, 871–885.

Xu, B., Noel, M., 1993. On the completeness of data sets with multielectrode systems for electrical resistivity survey. Geophys. Prospect. 41, 791–801.